CRYSTAL GROWTH & DESIGN

Article

pubs.acs.org/crystal

Molecular Dynamics Electric Field Crystallization Simulations of Paracetamol Produce a New Polymorph

Conor Parks,[†] Andy Koswara,[†] Hsien-Hsin Tung,[‡] Nandkishor Nere,[‡] Shailendra Bordawekar,[‡] Zoltan K. Nagy,[†] and Doraiswami Ramkrishna*[,†]

[†]School of Chemical Engineering, Purdue University, 480 West Stadium Mall, West Lafayette, Indiana 47907, United States

[‡]Process Research & Development, AbbVie, Inc., 1 North Waukegan Road, North Chicago, Illinois 60064, United States

Supporting Information

ABSTRACT: Using molecular dynamics simulations, we demonstrate the ability of high intensity, 1.5 V/nm, static electric fields to induce the formation of a new polymorph of paracetamol, one of the most important fever and pain suppressants in the world. In the newly produced polymorphic form, paracetamol molecules adopt a spatial orientation that maximizes the alignment between the electric dipole and the applied electric field vector. As the properties of crystalline materials are ultimately determined by the conformational and packing patterns of molecules in the solid state, it is predicted that electric fields have the potential to spur the creation of never before seen materials with potential novel properties such as increased drug efficacy in vivo. Paracetamol nanocrystal growth and dissolution dynamics are systematically investigated as a function of the applied electric field intensity and temperature. It is shown that the electric field suppresses the growth rate of supersaturated paracetamol nanocrystals, and can both increase and inhibit the dissolution rates of undersaturated paracetamol nanocrystals. This shows that molecular dynamics predicts that electric fields are a useful control variable for the manipulation of crystal size distributions and crystallization dynamics. Analysis of the crystal morphology under the presence of the electric field shows that paracetamol nanocrystals adopt an electric field intensity dependent morphology. Finally, the new polymorph is shown to be metastable in the absence of the electric field with increased aqueous solubility and hence potentially bioavailability relative to form I and II. The new form is stabilized at short times through a temperature quench, but requires longer application of the electric field to maintain the new polymorph during crystallization.

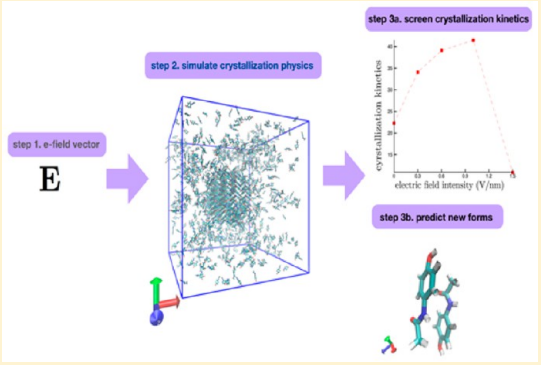

1. INTRODUCTION

New methods for the production of a targeted crystalline material stand ready to impact industries as diverse as pharma, energy, and defense. In the pharmaceutical industry for example, the polymorphic form determines all key physical characteristics of orally administered drug tablets such as compactability, solubility, bioavailability, shelf life, and growth and dissolution rate.[1] Molecules can pack into different molecular motifs, a phenomenon known as packing polymorphism, or can adopt different conformations to produce a conformational polymorph.[2] Even subtle variations in the conformation adopted by the molecules in the solid state can have dramatic impacts on solid state characteristics, as displayed by the HIV drug ritonavir.[3] The variety of physical characteristics displayed by different polymorphs is further illustrated by the molecule paracetamol (acetaminophen), one of the most widely used antipyretic (fever suppressant) and analgesic (pain suppressant) drugs in the world.[4] Paracetamol crystallizes readily from aqueous solution into the globally stable form I characterized by a herringbone arrangement of paracetamol molecules in the solid state. However, the metastable form II displays higher aqueous solubility and bioavailability, and is more readily compressible into tablets due to the layered sheets packing of the molecules in form II.[5] The improved tableting performance of form II makes it highly desirable commercially, as a costly wet granulation unit operation is no longer necessary as in the case of form I.[6] Methods to crystallize form II in sufficiently high purity are still an active field of research,[5] as form II undergoes a solvent mediated solid state transition to the less soluble form I.[7] This displays how current polymorph control crystallization strategies can be insufficient and difficult to implement, and can fail to access even the various low energy structures a molecule can adopt in the solid state.[4] New methods to produce a wider range of crystalline materials include bottom up nanocrystallization strategies which have shown remarkable progress at crystallizing a larger subset of the low energy metastable forms through thermodynamic and crystallization chamber size manipulation.[8−11] However, an externally applied electric field (efield) allows for direct manipulation of the underlying crystallization energy landscape,

Received: March 10, 2017
Revised: May 3, 2017
Published: June 7, 2017

DOI: 10.1021/acs.cgd.7b00356
Cryst. Growth Des. 2017, 17, 3751−3765

and can modulate the kinetic barriers preventing the formation of novel materials. As such, externally applied fields may be useful to further extend the set of obtainable crystal structures to encompass many more of the 230 possible space groups from crystallography, and reveal the full set of physical characteristics a molecule can display in the solid state.

Molecular dynamics (MD) based simulations allow for the screening of efield variables to quantitatively assess the impact on the crystallization dynamics, crystal morphology, and polymorph structure, with fully atomistic resolution. In the classical limit, the electric field induces forces to align the dipole moment of a molecule with the applied electric field vector according to Lorentz law, shown for a field with no magnetic component in eq 1:

$$\boldsymbol{F}_{i-ef}(t) = \sum_{k=1}^{N_T} q_k \cdot \mathbf{E}(\mathbf{r}, t) \tag{1}$$

where $\boldsymbol{F}_{i-ef}$ (t) is the total electric field induced force on molecule i, N_T is the number of atoms in the molecule, q_k is the charge of atom k, and $\boldsymbol{E}(\boldsymbol{r}, t)$ is the efield vector at coordinate vector $\boldsymbol{r}$ and time t. Equation 1 can be equivalently viewed from the perspective of the Hamiltonian where the application of an efield adds a perturbation term seeking to align the dipole moment of the molecule with the efield vector, displayed in eq 2:

$$H_e(t) = -|\boldsymbol{\mu}_0||\mathbf{E}(\mathbf{r}, t)|\cos(\theta) \tag{2}$$

where $H_e(t)$ is the time dependent efield contribution to the Hamiltonian, $\boldsymbol{\mu}_0$ is the permanent dipole moment vector of the molecule, and θ is the angle between $\boldsymbol{\mu}_0$ and $\boldsymbol{E}(\boldsymbol{r}, t)$. Through its time and spatially varying induced forces as permitted by the Maxwell's equations, the efield allows for spatial and temporal control at the atomic level over the conformations and spatial orientations a molecule can adopt, thus allowing for potential control of the nucleation, growth, and dissolution kinetics in addition to the polymorphic form. Two decades ago, it was discovered experimentally that intense pulses of near-infrared from a laser could induce the nucleation of supersaturated urea solutions.[12] At the same time, MD simulations showed 5 V/nm intensity efields induced homogeneous tip4p water nucleation within 200 ps,[13] producing the metastable ice I_c at atmospheric pressures,[13] and a new quartz like polymorph at 3−5 kbar.[14] Experimentally, it was demonstrated that linear and circular efield polarizations induce the nucleation of different polymorphs of the amino acid glycine[15] and L-histidine.[16] Static efields, also known as DC efields, were shown to induce the formation of the γ-polymorph of glycine from aqueous solution,[17] whereas α- crystallizes in the absence of an applied efield.[18] Through MD simulations, heterogeneous ice nucleation was found to be accelerated through the application of 1.5−3.5 V/nm intensity efields using the six-site and tip4p/ICE water models, suggesting the local efields may be a significant factor controlling heterogeneous ice nucleation in nature.[19] In homogeneous nucleation studies, MD simulations predicted that the melting temperature of ice I_c crystals were elevated upward of 40 K when exposed to 1−2 V/nm intensity efields using the six-site water model.[20] This was attributed to the near perfect alignment between the ice I_c molecules and the applied efield vector. Experimentally, a field strength 10^4 times weaker showed no acceleration in the nucleation kinetics of ice,[21] demonstrating how the electric field induced forces compete with intrinsic forces present in the unperturbed molecular Hamiltonian, and may only become relevant with sufficiently high efield intensity. In addition, the success of the efield vector to manipulate the crystallization pathway may be solute dependent, as the magnitude of the dipole moment will vary between organic molecules. For instance, being a zwitterion, glycine has a large molecular dipole of 9.98 D (estimated using CNDO charges[22]) making it respond readily to the application of an efield. By contrast, paracetamol has a much lower molecular dipole of 4.52 D (estimated using AM1-BCC charges[23]). Recent magnetic field crystallization experiments of paracetamol have demonstrated that paracetamol crystallization kinetics is in fact decelerated by the application of the external field, and form I still crystallized from solution.[24] To date, no MD efield crystallization simulations have been performed on organic molecules in solution. The in silico screening of electric field parameters of pharmaceutically relevant compound will aid in the quest to not only understand the impact of an efield on the crystallization process, but also to discover new polymorphic forms with potentially novel crystal properties.

Motivated by the above considerations, we sought to systematically explore the impact of an externally applied efield vector on the paracetamol nanocrystal dissolution and growth dynamics, crystal morphology, as well as polymorphic form produced. In the simulation details section, the rational behind the selection of the efield vectors chosen in this work, and the computational procedure to screen both crystallization kinetics and polymorphic structure as a function of the applied efield intensity is discussed. In the Results and Discussion, the crystallization growth and dissolution rates, time series alignment data, polymorphic form analysis, morphology analysis, temperature quench data, and consideration for experimental testing are presented. In the Conclusion, the general findings and implication of the work for the crystallization of targeted materials are discussed.

2. SIMULATIONS DETAILS

MD simulations were performed using an in-house MD code designed for Intel Xeon Phi coprocessor hardware and the embarrassingly parallel nature of crystallization trajectories. Details of the code employed can be found in the literature.[25] The code can be obtained either through github[26] or by contacting the authors. The GAFF[23] force field with AM1-BCC charges were used for paracetamol, and the tip3p water model was used for water, as this force field combination has been shown to accurately reproduce the enthalpy of solvation of paracetamol crystals in aqueous solution.[27] The AM1-BCC charges are shown graphically in Supplementary Figure 1, Supporting Information. The ability to reproduce the sign of the enthalpy of solvation has been shown to be critical to the ability to simulate crystal growth,[22] as otherwise it is thermodynamically impossible for crystal growth to occur.

Short-range nonbonded forces were truncated at 0.9 nm in agreement with the GAFF force field.[27] Reciprocal space electrostatic forces were computed using a particle mesh Ewald (PME) solver with a 1×10^{-6} error tolerance. 132 grid points were used in each direction for the PME solver. The temperature was controlled using a Langevin thermostat with a relaxation time of 2000 fs. The isotropic Berendsen barostat was used with a 1000 fs relaxation time and a set point of 1 atm. A value of 21454.85 atm was used for the bulk modulus of water to determine the relaxation time constant in the Berendsen barostat. The shake algorithm was employed to

DOI: 10.1021/acs.cgd.7b00356
Cryst. Growth Des. 2017, 17, 3751−3765

constrain the motion of all bonds containing hydrogen. A shake tolerance of 1×10^{-4} was employed for all simulations, and a maximum number of 25 shake iterations were allowed. Periodic boundary conditions were employed in all directions. A cubic simulation box was employed in all simulations. The equations of motion were set as shown in eq 3:

$$m\ddot{\mathbf{r}}_i = \boldsymbol{F}_i + q_i\mathbf{E}(\mathbf{r}, t) \tag{3}$$

where q_i denotes the partial atomic charge of atom i. Equation 3 was solved using a velocity Verlet algorithm with a 3 fs time step.

To prepare an initial configuration of paracetamol and water molecules for liquid phase equilibration, 1200 paracetmol molecules were inserted into a 12.5 nm cubic box using the gromacs/5.0[28] insert molecules command. The box was then solvated with water molecules using the gromacs/5.0 solvate command. This led to 51 691 water molecules being inserted into the box. The energy of the system was then minimized in gromacs/5.0, using steepest descent minimization, with an energy minimization tolerance of 100 kJ/mol/nm. The fluid was then equilibrated in the NVT ensemble at 380 K for 7 ns. The fluid was next equilibrated in the NPT ensemble at 1 atm for 7 ns.

A form I spherical nanocrystal with a 2.9 nm radius was sliced form the bulk structure obtained from the Cambridge Crystal Structural database.[29] The nanocrystal was imbedded in the equilibrated fluid using the gromacs/5.0 solvate command. The energy of the nanocrystal embedded in fluid system was then minimized in gromacs/5.0, using steepest descent minimization, with an energy minimization tolerance of 100.0 kJ/mol/nm. Ten trajectories were then launched from the nanocrystal plus solute/solvent liquid system in an embarrassingly parallel multiple replica strategy[25] at the temperature and field intensity of interest. Simulations were performed for 6.3 ns. The results from all 10 trajectories were then averaged to provide average growth and dissolution kinetics. Dissolution and growth rates were calculated through linear fits to the final 5.3 ns of simulation trajectory.

At the beginning of production runs, a static efield was applied in the x direction with no component in the y and z direction. A static field was chosen as the interaction between the molecule and the efield would be mainly due to its classically defined permanent dipole such that higher order dipole terms, which are quantum mechanical in nature, and hence not captured in the GAFF[23] + tip3p molecular force field used in this work, can be neglected.[30] An exhaustive efield screening was performed by simulating static efield strengths of 0 V/nm (no field), 0.3 V/nm, 0.6 V/nm, 1 V/nm, and 1.5 V/nm. The effect of temperature was studied by performing all efield intensity simulations both at 300 K (supersaturated) and 370 K (undersaturated). The selection of these field intensities allows us to study both linear and nonlinear regime dynamics.[31] These field intensities are larger than what has been experimentally applied to crystallization systems to date, but are in line with efield intensities frequently implemented in MD studies, as discussed in the introduction.

As done previously in the literature for other molecules, such as glycine[32−34] and NaCl,[35] paracetamol molecules were labeled either solid or liquid based on the local density of the molecule. With the given force field, the density of bulk form I is 1.26 g/cm^3, or 9 paracetamol molecules in a 0.75 nm radius sphere. To allow for thermal fluctuations and a diffusive density distribution in solution, a paracetamol molecule was labeled solid if it possessed eight or more paracetamol neighbors in a 0.75 nm radius sphere. Distances between paracetamol molecules were calculated between centroids of the two molecules. A distance of 0.75 nm was chosen as this corresponds roughly to the first minimum in the paracetamol-paracetamol radial distribution function in solution, and showed good ability to identify the correct number of solid molecules for paracetamol nanocrystals. Surface molecules were included in the clustering algorithm by counting a molecule as solid if it had a neighbor who met the density criterion, but did not meet the density criterion itself. The number of solid molecules in the largest cluster, n, was then calculated through a clustering algorithm that counted all solid molecules that were also separated by less than a specified cut off distance. As shown in Supplementary Table 1, this procedure produced near perfect agreement between the number of molecules in our initial nanocrystals and the predicted n. For data analysis, n was calculated at a 3 ps interval. This method of solid molecule recognitions lacks the ability to identify polymorphic forms. Therefore, crystal structures were analyzed through post processing and visual analysis.

To analyze the morphology of the nanocrystals as a function of the applied efield intensity, the sphericity of the particles was calculated through the eigenvalues of the moment of inertia tensor of the paracetamol nanocrystals.[36] The sphericity, S, is defined to be the ratio of the minimum and maximum eigenvalues, $\lambda_{min}/\lambda_{max}$, of the moment of inertia tensor. For a perfectly spherical particle, the eigenvalues of all three eigenvectors will be equal, and S will be equal to 1. Deviations from unity provide insight into the effect of the applied efield vector on the resulting morphologies adopted by paracetamol nanocrystals along the crystal dissolution and growth pathways. Furthermore, the ratios of λ_x/λ_z, λ_y/λ_z, and λ_x/λ_y allow the minimum eigenvalue to be determined, which in turn conveys the principal axis (axis corresponding to minimum eigenvalue). This allows for a quantitative analysis of the preferred growth and elongation axis of the simulated nanoparticles as a function of the applied efield intensity. In addition to sphericity analysis, the eigenvalues are subjected to the method of analysis performed by Sikora et al.[37] Here, effective radii are defined according to eq 4.

$$R_\lambda = \sqrt{\lambda/n} \tag{4}$$

where λ has three values corresponding to each eigenvector, and n is the number of molecules in the solid cluster. The three radii parameters can be combined to yield one parameter w for analysis, displayed in eq 5:

$$w = \frac{\Delta R}{\overline{R}} \tag{5}$$

where $\Delta R = R_2 - \overline{R}$, $\overline{R} = 0.5(R_1 + R_3)$, and R_1, R_2, R_3 are the minimum, intermediate, and maximum values of R_λ. As outlined in the literature, negative values of w correspond to plate-like morphologies, and positive values correspond to cigar-like morphologies.[37] The sphericity analysis allows analyzing any deviations from the initial spherical particle morphologies, and analysis of w allows for the characterization of either cigar-like, or plate-like morphologies for particles that demonstrate deviations from near unity values of S.

To perform temperature-screening simulations, the efield was instantaneously turned off, the velocities were reinitialized according to a new, lower, set point temperature, and

DOI: 10.1021/acs.cgd.7b00356
Cryst. Growth Des. 2017, 17, 3751−3765

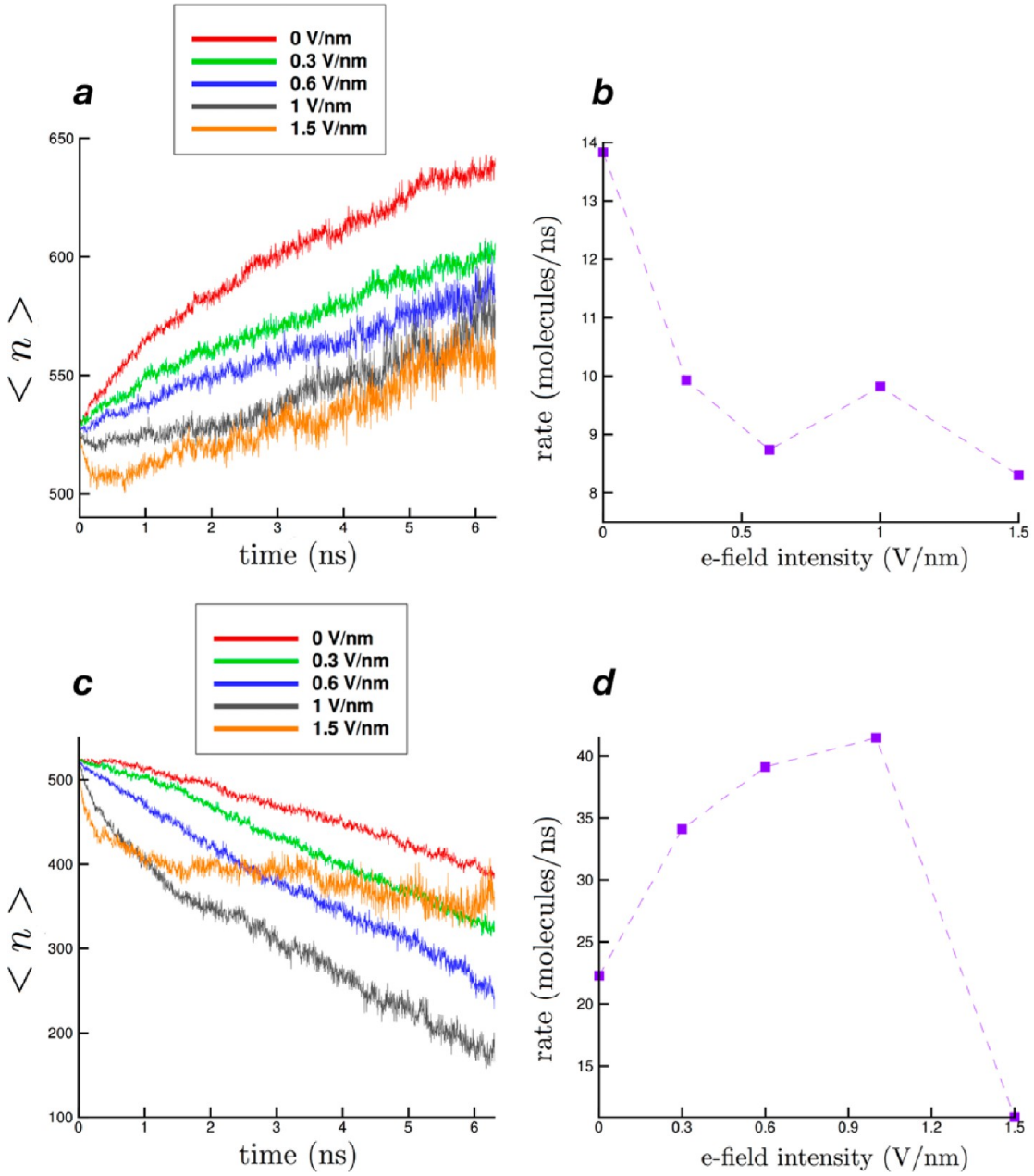

Figure 1. (a) Average number of crystal molecules, $\langle n \rangle$, against time (ns), for each efield intensity at 300 K. (b) Average growth rates (molecules/ns) at 300 K determined through linear fit analysis. (c) Average number of solid molecules, $\langle n \rangle$, against time (ns), for each efield intensity at 370 K. (d) Average dissolution rates (molecules/ns) at 370 K determined through linear fit analysis.

simulations were continued in the absence of the efield for an additional 6.3 ns. This procedure was performed for the nanocrystals grown at 300 K in the presence of the 1.5 V/nm intensity efield.

3. RESULTS AND DISCUSSION

In the sections below, the results for the growth and dissolution kinetics, alignment, polymorphic form, morphology and temperature quench are presented.

3a. Dissolution and Growth Rate Analysis. In Figure 1, the average n is displayed for each efield intensity and temperature simulated, along with the estimated growth and dissolution rates. In the 300 K temperature case, the efield is found to impede crystallization growth rates. The fastest predicted growth rate occurs in the no field case at an estimated rate of 13.8 molecules/ns, and the minimum predicted growth rate occurs in the 1.5 V/nm intensity simulation at a rate of 8.3 molecules/ns. In total, it is found that the efield reduces the crystallization growth rate by 40% over the range of intensities simulation. Little to no variation in the crystal growth kinetics is found with increasing efield past 0.3 V/nm. It is worth noting that the observation that an externally applied field impedes crystallization growth rates is consistent with paracetamol magnetic field crystallization experiments, though, for the latter, the mechanism may be different in terms of the field alignment with the molecule's magnetic dipole. Experimentally, it was observed that the nucleation rate induction time measurements of paracetamol were reduced by up to a factor of 2 by the application of a magnetic field with a 510 G field intensity.[24]

DOI: 10.1021/acs.cgd.7b00356
Cryst. Growth Des. 2017, 17, 3751−3765

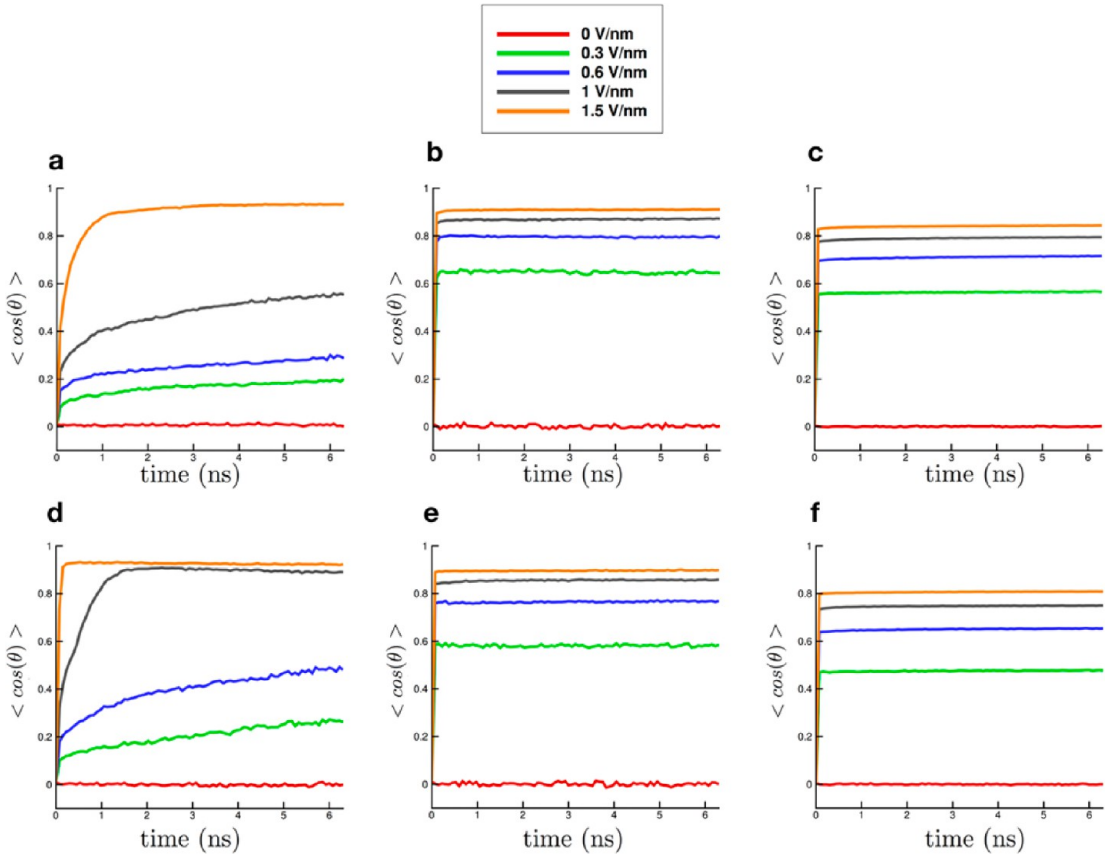

Figure 2. Average alignment, $\langle \cos \theta \rangle$, with the efield vector for each efield intensity in the case of (a) solid paracetamol molecules at 300 K, (b) liquid paracetamol molecules at 300 K, (c) water molecules at 300 K, (d) solid paracetamol molecules at 370 K, (e) liquid paracetamol molecules at 370 K, (f) water molecules at 370 K.

Contrary to the 300 K growth dynamics case, the dissolution dynamics at 370 K are shown to respond strongly to the applied efield in a non-monotonic manner. Relative to the no field dissolution rate of 22.9 molecules/ns, the dissolution rate first increases monotonically to its maximal value of 41.5 molecules/ns at 1 V/nm, a roughly 200% increase, relative to the no field dissolution rate. However, the dissolution rate is then found to decrease strongly with increasing efield intensity. The dissolution rate at 1.5 V/nm is found to only be 10.9 molecules/ns. This shows that the dissolution rates decreases by 75% over the 1−1.5 V/nm efield intensity window and achieves a dissolution rate that is 50% of the no-field dissolution rate. Therefore, the efield is predicted to provide significant control over the dissolution dynamics of paracetamol nanocrystals in aqueous solution.

3b. Efield Induced Alignment Analysis. To explain the observed growth and dissolution dynamics response to the applied efield, we analyze the time series alignment data generated during the course of the simulation. The response dynamics, for all temperatures and efield intensities for both liquid and solid paracetamol molecules, is displayed in Figure 2.

The alignment in the liquid and solid phase is shown to be a monotonically increasing function of the applied efield intensity at both temperatures. Liquid phase paracetamol and water molecules are shown to display rapid reorientation dynamics, assuming the steady state aligned orientations within the first 25 ps of simulation. In agreement with the paracetamol (∼4.52 D) > tip3p water (∼2.52 D) ranking of dipole moments, liquid paracetamol molecules are shown to adopt higher degrees of alignment with the efield vector than water molecules for all efield intensities and temperatures simulated. Rapid reorientation dynamics and monotonically increasing alignment with efield intensity is analogous to previous MD water efield simulations.[38] The average alignment decreases slightly between the 300 to 370 K simulations for liquid paracetamol and water molecules. This shows how thermal fluctuations compete with the efield induced forces seeking to align molecules. However, the opposite trend is observed for solid state paracetamol molecules, where solid paracetamol molecules are able to achieve higher values of alignment at 370 K than 300 K. This suggests that solid state paracetamol molecules must overcome an energy barrier to reorient with the applied efield vector. At higher temperatures, the thermal energy of molecules is larger, allowing for a more facile barrier crossing. Solid paracetamol molecules display slow reorientation dynamics, in comparison to the liquid, and steady state alignment values are only obtained in the 1.5 V/nm efield intensity simulation at 300 K, and the 1 V/nm and 1.5 V/nm simulations at 370 K. In the case of no field, no alignment on average is shown in either the liquid or solid phase at either temperature.

At 300 K, It is found that the liquid molecules obtain higher alignment values on average than solid molecules for the 0.3 V/nm, 0.6 V/nm, and 1 V/nm intensity efield simulations. By aligning more preferably with the applied efield vector, the liquid phase paracetamol molecules become stabilized relative to the solid, as the efield contribution to the molecular Hamiltonian, eq 2, increasingly favors the liquid phase, where

DOI: 10.1021/acs.cgd.7b00356
Cryst. Growth Des. 2017, 17, 3751−3765

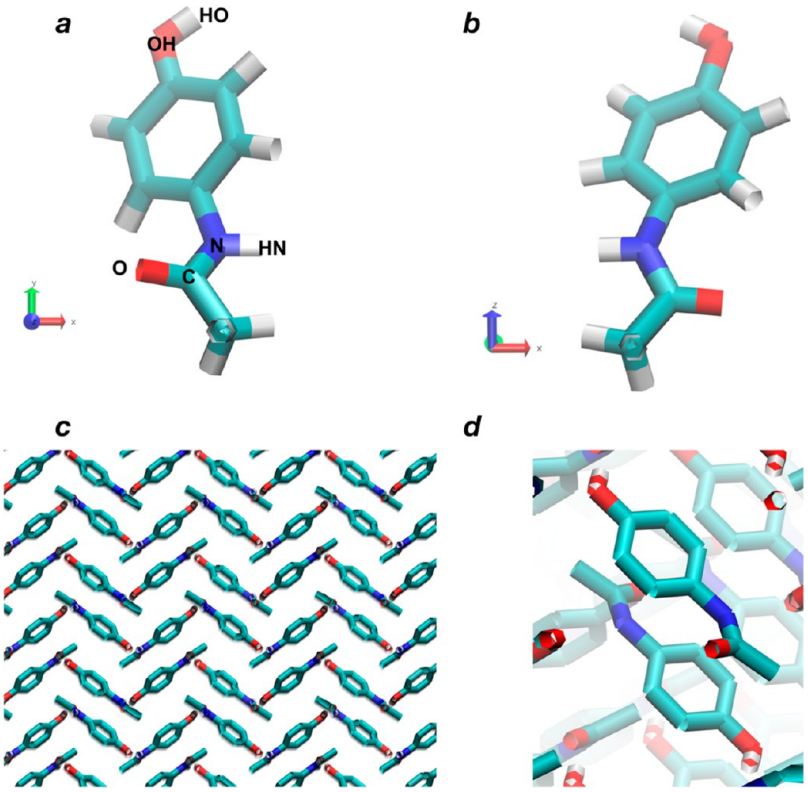

Figure 3. (a) Paracetamol with $\langle \cos \theta \rangle = 1$ with respect to x axis. (b) Paracetamol with $\langle \cos \theta \rangle = -1$ with respect to x axis. (c) Herringbone packing pattern of paracetamol form I taken from 0 K crystal structure. (d) Packing pattern of paracetamol pairs in form I taken from 0 K crystal structure. Hydrogens are not shown for clarity in c and d.

the dipole moments of liquid molecules align preferably with the efield vector. This rationalizes in part the observed growth rates as a function of the applied efield. As the solid is not able to adopt a more favorable configuration than the liquid in the presence of the applied efield, the driving force for crystal growth, the stability difference between the metastable liquid and stable solid, is reduced. Thus, the growth rate is lowered. In the 1.5 V/nm intensity simulations, solid and liquid molecules obtain nearly the same degree of alignment in the presence of the efield. As such, the depression in the observed growth rate relative to the no field simulation is likely due to effects at the liquid solid interface. In general, the growth of crystals proceeds through two mechanisms: (1) diffusion to the solid interface driven by the chemical potential difference between the solid and the liquid paracetamol molecules and (2) attachment of liquid paracetamol molecules to the solid determined by the ability of the liquid molecule to adopt a suitable molecular conformation and spatial orientation for binding with solid molecules at the interface. As the conformational and rotational entropy of the molecules is significantly reduced due to the presence of the efield, liquid paracetamol molecules may not be able to adopt a molecular conformation or spatial orientation suitable for attaching to the crystal at a 1.5 V/nm efield intensity.

At 370 K, the liquid molecules reorient and adopt orientations with higher alignment with the efield in the 0.3 V/nm and 0.6 V/nm intensity efield simulations than the solid phase. As the system is initially undersaturated at this temperature, exhibited by the dissolution of the nanoparticle in the no field case, preferable liquid orientations with the efield have the effect of stabilizing the liquid relative to the solid, and hence accelerating the dissolution of the nanoparticle. The solid molecules adopt more aligned orientations in the case of the 1 V/nm and 1.5 V/nm simulations. However, there is a time delay in obtaining the steady state alignment value in the 1 V/nm efield intensity simulation. In the 1 V/nm simulation, the solid molecules do not obtain a steady state value until 1.5 ns and do not adopt a more favorable configuration than the liquid until 1 ns. During the first 1 ns of simulation with the 1 V/nm intensity efield, the cluster dissolves to a size at which it is subcritical, forcing it to dissolve for the remainder of the simulation,[34,39−44] despite obtaining a higher degree of alignment than the liquid. During the 1.5 V/nm intensity simulation, solid molecules reorient as quickly as the liquid molecules and obtain a higher degree of alignment. This rationalizes the depression in the dissolution dynamics observed in the 1.5 V/nm intensity efield simulation, as the solid state molecules are stabilized relative to the liquid in the presence of the 1.5 V/nm intensity efield. The stabilization of the solid-phase reduces the driving force for dissolution, i.e., the difference in stability between the stable liquid and the metastable nanocrystal.

The question of whether electrofreezing of the tip3p water molecules is contributing to the observed growth and dissolution rates must also be addressed in addition to the alignment. Yan, Overduin, and Patey studied the electrofreezing of water using the six-site water model which has a reported melting temperature of 289 K.[20,45] It was observed that efield strengths between 1 and 2 V/nm could induce the electrofreezing of the six-site water model within 50 ns at 270 K; however no freezing was observed at 280 K. The melting temperature of the crystallized ice I_c nanocrystals was raised by

DOI: 10.1021/acs.cgd.7b00356
Cryst. Growth Des. 2017, 17, 3751−3765

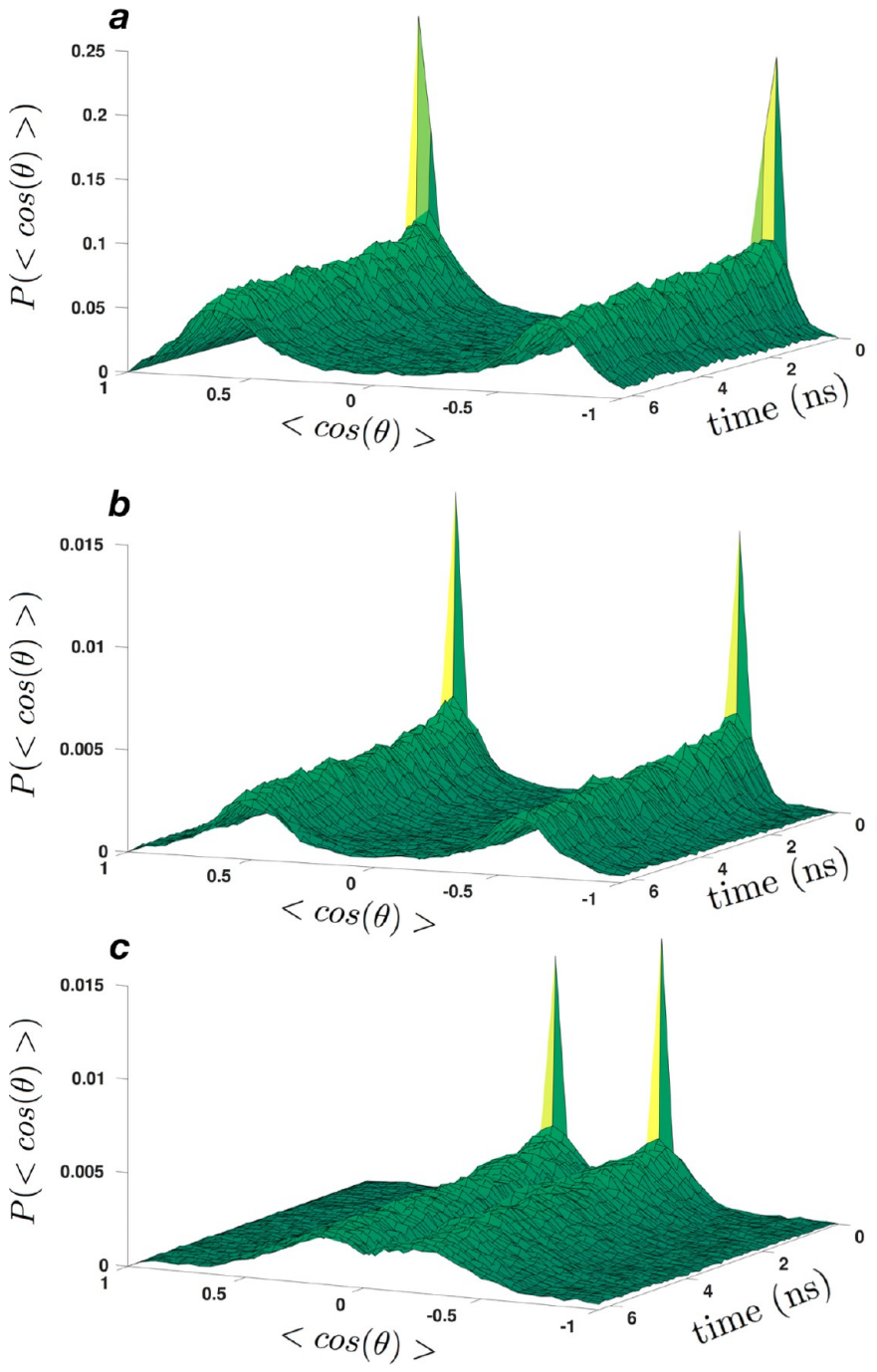

Figure 4. Probability distribution of <cos θ>, where θ is angle between (a) N−HN, (b) O−C, and (c) OH−HO bond vector and the efield vector, during the no-field simulation, vs time (ns). Each <cos θ> is averaged over all 10-simulation trajectories.

36 deg in the presence of the 1.5 V/nm efield due to the optimal alignment of ice I_c molecules with the applied efield vector. However, the tip3p water model melting temperature used in this work is only 145.6 K,[46] making it highly unlikely that the efield strengths in this work could induce freezing in the presence of dissolved solute at 300 K, as the melting temperature of ice would need to be raised by more than 155 K by the efield. To check if electrofreezing of water contributed to the results herein, a radial distribution function (RDF) analysis was performed. The radial distribution function of water molecules was calculated for the 0 V/nm and 1.5 V/nm intensity simulations at 300 K and are shown in Supplementary Figure 2. This was done to discern if any RDF peaks corresponding to ice I_c was observed in the 1.5 V/nm intensity simulation. We do not observe elevated peaks between 4 and 5 Å characteristic of ice I_c,[47] and the 1.5 V/nm RDF shows similarity to the 0 V/nm RDF. As such, electrofreezing of water is not believed to contribute to the results stated herein.

3c. Polymorphic Form Analysis. To understand the spatial orientations and molecular conformations of paracetamol molecules adopted in the aligned states in Figure 2, due to the presence of the efield, we begin by analyzing Figure 3a,b which shows paracetamol molecules with net dipoles corresponding to alignment, $(\cos(\theta) = 1)$, and antialignment, $(\cos(\theta) = -1)$, with respect to the x-axis, and hence efield vector. Analysis of the two structures shows that the dipole

DOI: 10.1021/acs.cgd.7b00356
Cryst. Growth Des. 2017, 17, 3751−3765

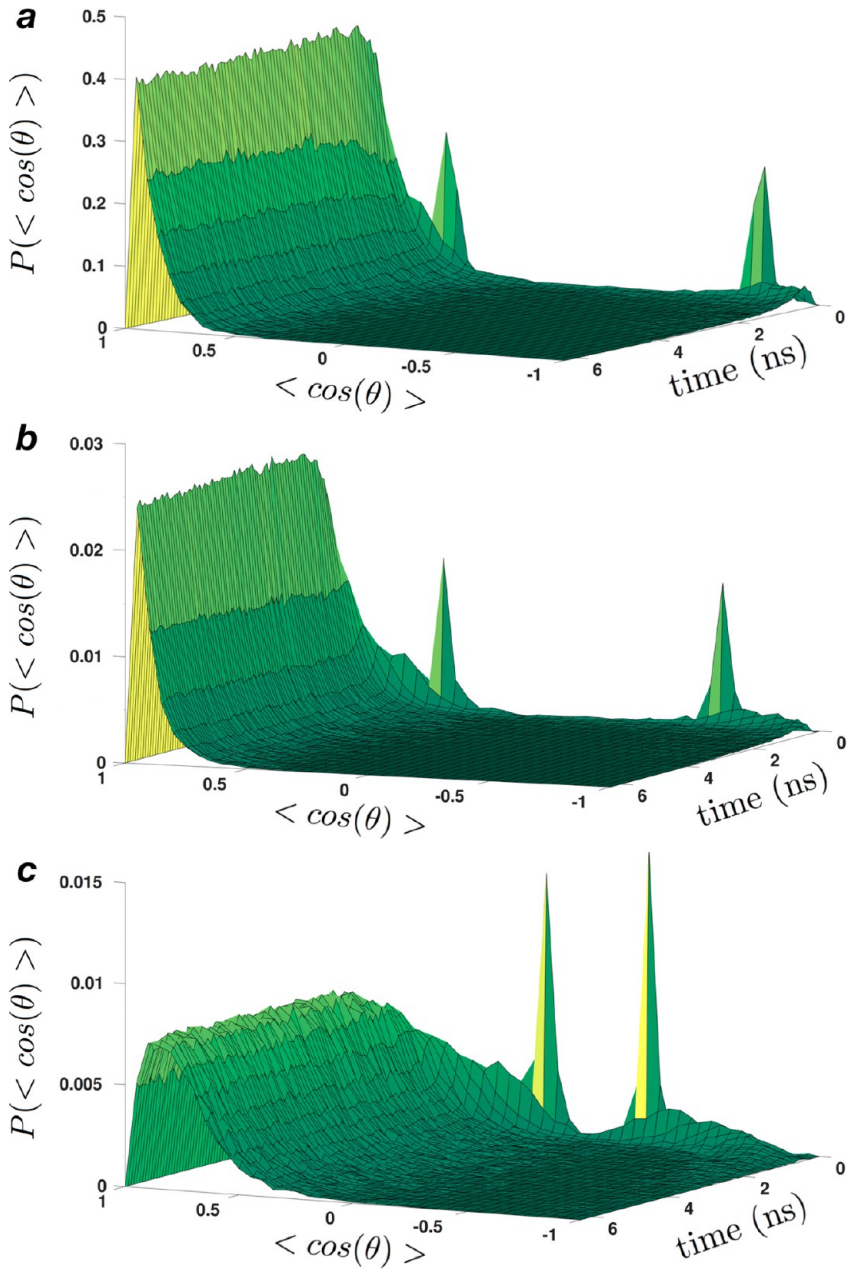

Figure 5. Probability distribution of <cos θ>, where θ is angle between (a) N−HN, (b) O−C, and (c) OH−HO bond vector and the efield vector, during the 1.5 V/nm intensity efield simulation, vs time (ns). Each <cos θ> is averaged over all 10-simulation trajectories.

alignment with the external efield, along the x-axis, is determined by the angle between the applied efield, and the bond vectors with the largest charge separations between atoms forming the bond: the OH−HO, N−HN, and O−C bond vectors (atoms are labeled in Figure 3a to aid the reader).

In the form I polymorph, paracetamol molecules stack in a herringbone tiling pattern, characterized by pairs of paracetamol molecules tilted down two unique axes, displayed in Figure 3c. Visual analysis of an individual pair in Figure 3d shows that the paracetamol molecules pack with antiparallel OH−HO, N−C, and O−C bonds with respect to each other. As such, the application of an external efield will result in the bonds in one molecule favoring efield alignment and bonds in the other molecule favoring anti efield alignment.

In Figure 4, we plot the temporal evolution of the probability distribution for $\langle \cos \theta \rangle$ between the N−HN, O−C, and OH−HO bond vectors and the x-axis in the case of the no field simulation at 300 K. At t = 0, strong bimodal peaks corresponding to the bulk crystal structure are present, with one peak in phase with the x-axis (positive $\langle \cos \theta \rangle$), and one peak out of phase with the x-axis (negative $\langle \cos \theta \rangle$), in agreement with the observation that the N−HN, O−C, and OH−HO bonds pack antiparallel in Figure 3d. Thermal motion subsequently lowers the bimodal peak intensities, making the distribution broader and more diffuse. The distributions in Figure 4 are symmetric with respect to the $\langle \cos \theta \rangle$ axis, providing an explanation for the zero average alignment observed during the no-field simulations in Figure 2. Throughout the course of the simulation, the bimodal characteristic of the distributions, and locations of the bimodal peaks, is time invariant. These facts suggest that the form I packing pattern is retained in the absence of the efield. This is

DOI: 10.1021/acs.cgd.7b00356
Cryst. Growth Des. 2017, 17, 3751−3765

confirmed through visual analysis of the nanocrystals grown in the absence of the efield, which is demonstrated in Figure 6a, that show clearly the presence of form I.

In Figure 5, we plot the temporal evolution of the probability distribution for $\langle \cos \theta \rangle$ between the N−HN, O−C, and OH−HO bond vectors, and the applied efield vector, in the case of the 1.5 V/nm intensity efield simulation at 300 K. The strong bimodal peaks observed in Figure 4 are still present at $t = 0$, as these correspond to the initial form I polymorph embedded into the solution. However, the temporal evolution of the probability distributions is drastically different with the 1.5 V/nm intensity efield vector than in the no field simulation case. Rather than the bimodal distributions present in Figure 4, the distributions have become unimodal, implying the nature of the solid state packing of paracetamol molecules has been altered. The N−HN, O−C, and OH−HO bond distributions have shifted their means to $\langle \cos \theta \rangle \approx 1$, indicating that each bond has now reoriented and aligned its dipole with the applied efield. The new orientation of paracetamol bond vectors in the presence of the efield shows the formation of a new polymorph by definition.

In Figure 6a,b, we provide representative snapshots of the crystal lattices produced during the no-field and 1.5 V/nm intensity efield simulation, respectively. Both crystal lattices display the form I herringbone packing pattern; however the efield has created more stacking defaults in Figure 6b relative to 6a. The herringbone packing pair produced during the 1.5 V/nm intensity efield simulation is provided in Figure 6c. The molecular conformation of paracetamol molecules in the packing pair is equivalent to the form I pair in Figure 3d. However, rather than packing with antiparallel O−C, N−HN, and OH−HO bonds vectors, the molecule that was initially out of alignment with the efield vector adopts a new spatial orientation and aligns its dipole with the applied efield. As such, the fundamental building unit of the polymorph has undergone a solid state transition to align the dipole of each paracetamol molecule with the applied efield vector. This provides definitive evidence that a new polymorph of paracetamol has been created through efield induced dipole alignment maximization.

The creation of a polymorph whose alignment with the applied efield vector is maximized is in agreement with ice[13,19,20,48] nucleation simulations and is in agreement with the optical Kerr mechanism.[15,49] In MD simulations, it has been shown that ice I_c can coexist with water significantly above the melting temperature in the presence of 1−2 V/nm static efields.[20] This was attributed to the near perfect alignment of ice I_c molecules in the solid state. The application of 40 V/nm intensity efield induced the crystallization of an ordered, completely polarized ice-like structure which is laterally stabilized via hydrogen bonds.[48] Heterogeneous nucleation of ice has also been shown to produce ice I_c in the presence of an efield in MD.[19,50] However, recent work under partial band simulations, where the efield is restricted to regions of the surface upon which heterogeneous nucleation is occurring, may suggest that the efield induced formation of ice I_c may also be effected by nefarious artifacts of employing periodic boundary conditions. However, we do not anticipate any unphysical periodic boundary conditions in this work, as the polymorph produced is the result of a solid state transition and not a growth mechanism. Experimentally, recent work studying the crystallization of coronene has demonstrated that crystals grown under magnetic field strengths of 1 T produce a previously unknown polymorphic form, where the formation of the new polymorph was attributed to magnetic dipole maximization, analogous to the electric dipole maximization mechanism observed in this work.[51]

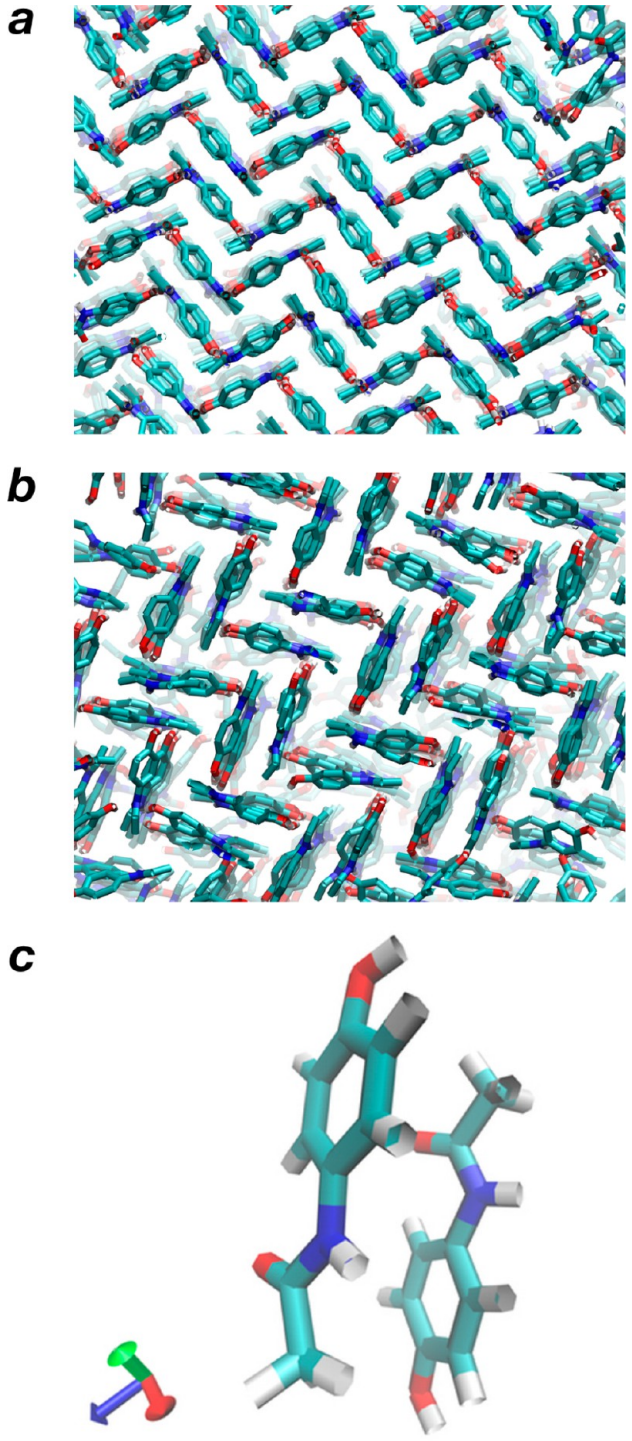

Figure 6. Snapshot of a final crystal structures produced during the (a) no efield and the (b) 1.5 V/nm efield intensity simulation, at 300 K. In plot (c) the packing pair of paracetamol grown in the presence of a 1.5 V/nm intensity efield, demonstrating the new polymorph is displayed. Contrary to the form I packing pair, the N−HN, O−C, and OH−HO bond vector now stack parallel with respect to each other, allowing the dipole moment of both molecules to point down the efield vector. In (a) and (b), the hydrogen atoms are not shown for clarity.

The findings in this work and those mentioned above suggest a general phenomenon predicted by MD that the application of

DOI: 10.1021/acs.cgd.7b00356
Cryst. Growth Des. 2017, 17, 3751−3765

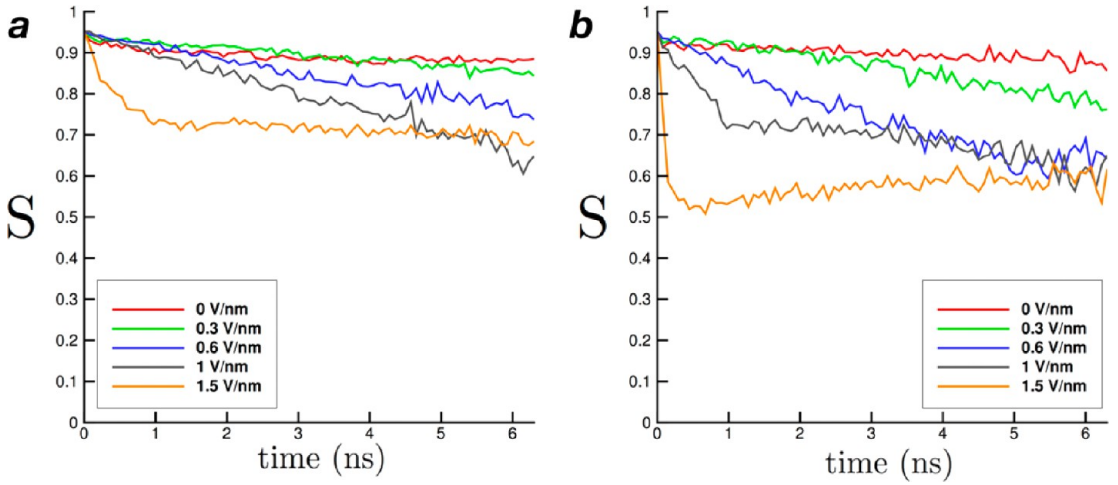

Figure 7. (a) *S* time-series data at 300 K, (b) *S* time-series data at 370 K.

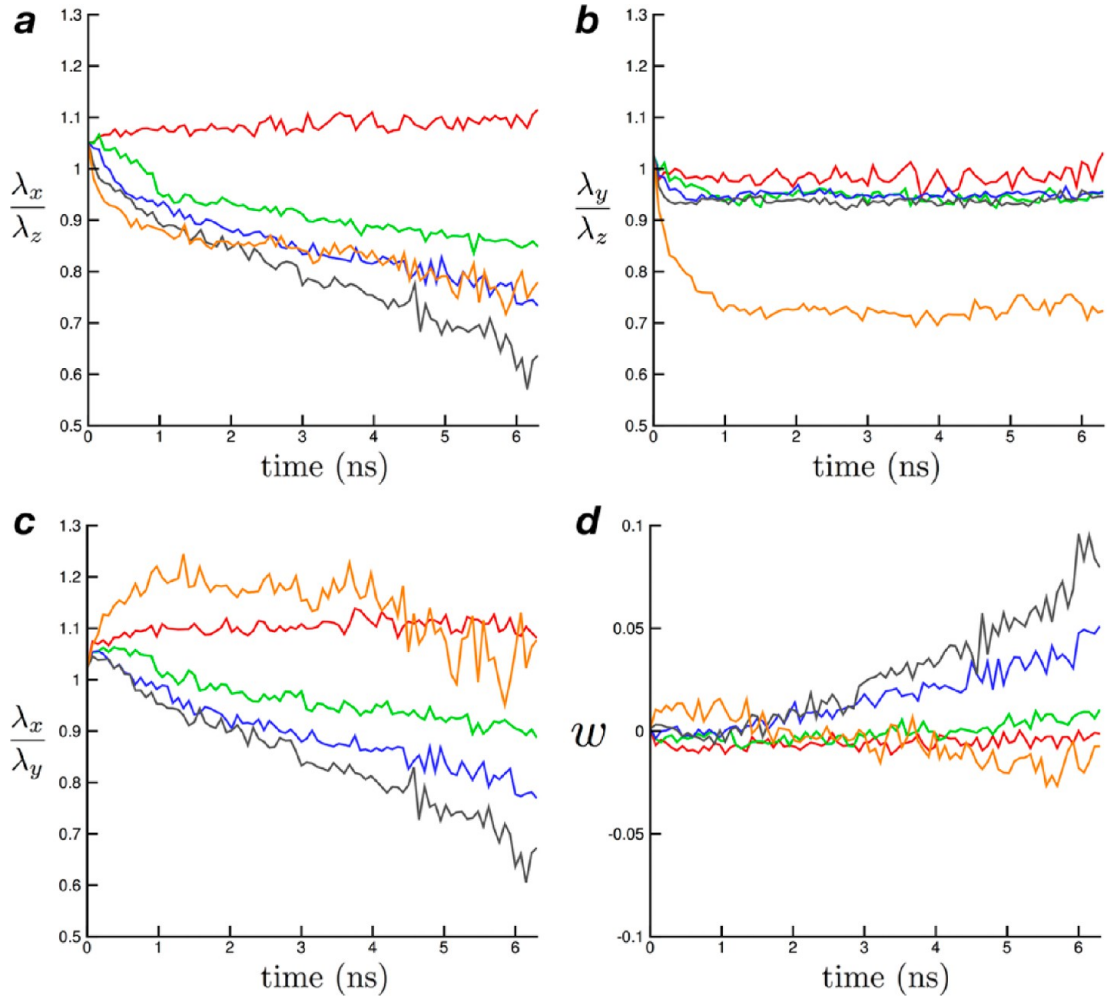

Figure 8. Eigenvalue analysis and morphology analysis for (a) λ_x/λ_z, (b) λ_y/λ_z, (c) λ_x/λ_y, and (d) w for the case of the no field (red), 0.3 V/nm (green), 0.6 V/nm (blue), 1 V/nm (gray), and 1.5 V/nm (orange) simulations at 300 K.

suitably high intensity static efields directs the formation of crystal structures that adopt suitable alignment with the applied efield. This is a straightforward and intuitive concept, as the classical effect of the applied efield is to maximize the alignment between the dipole of the molecule and the efield vector. With a suitably high efield intensity, the efield induced forces will overcome the intrinsic forces in the natural molecular Hamiltonian, and the solute, both in the solid and liquid phase, and solvent molecules will be forced to align with the efield. However, it remains to be proven whether the creation of new materials will manifest itself when quantum mechanical forces are taken into account. If this phenomenon is shown to

DOI: 10.1021/acs.cgd.7b00356
Cryst. Growth Des. 2017, 17, 3751−3765

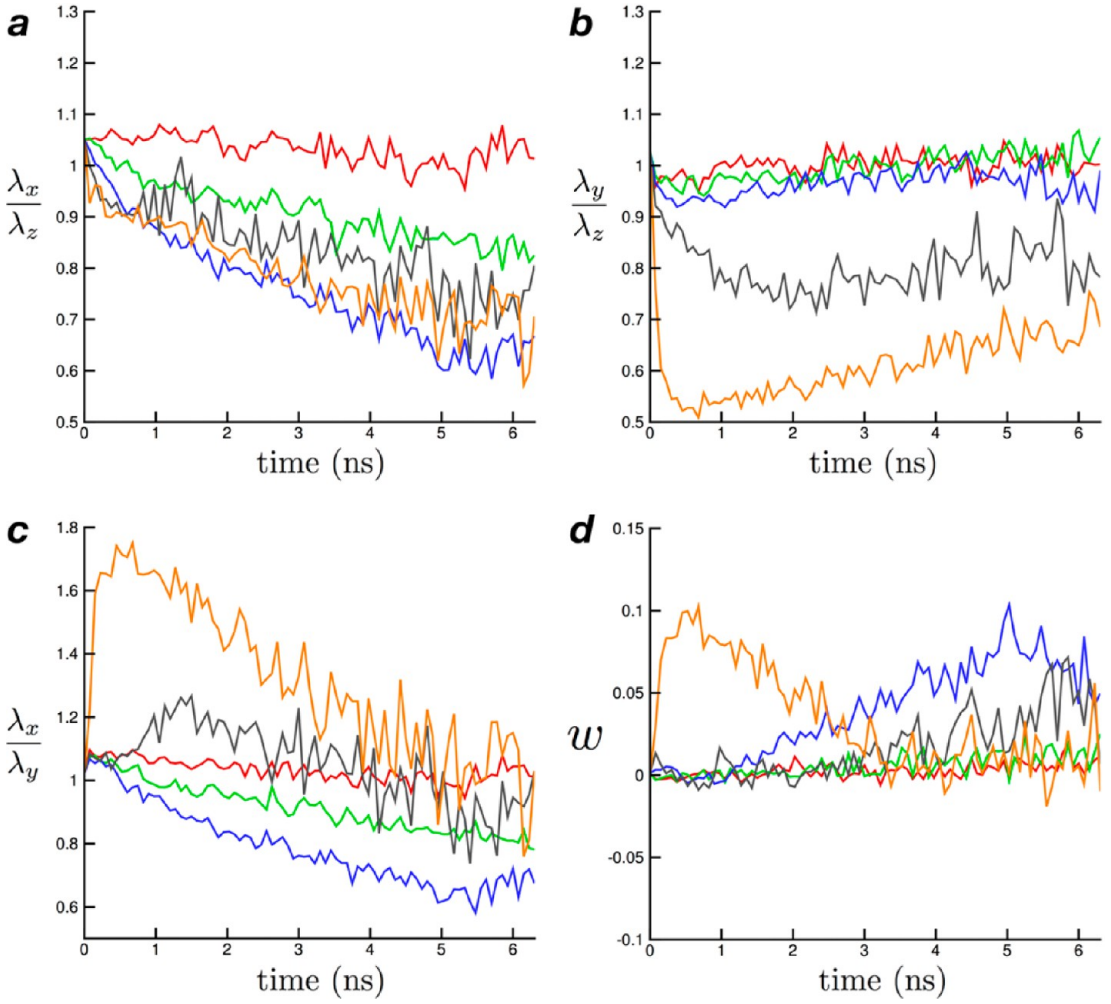

Figure 9. Eigenvalue analysis and morphology analysis for (a) λ_x/λ_z (b) λ_y/λ_z (c) λ_x/λ_y, and (d) w for the case of the no field (red), 0.3 V/nm (green), 0.6 V/nm (blue), 1 V/nm (gray), and 1.5 V/nm (orange) simulations at 370 K.

hold experimentally as well, this has the potential to allow for the formation of new materials with potentially improved solid state crystal properties, such as bioavailability.

3d. Nanocrystal Morphology Analysis. The time series sphericity data profiles for both the 300 and 370 K simulations are plotted in Figure 7a and 7b, respectively. In the no field case, the morphology of the paracetamol nanocrystal grows and dissolves through a highly spherical mechanism, indicated by the near unity of S. However, the sphericity is observed to be a monotonically decreasing function of the applied efield intensity. In the 1.5 V/nm efield simulation, the sphericity adopts an average value of $S = 0.7$ and $S = 0.6$ at 300 and 370 K respectively, at the conclusion of the simulation, providing a 23% and 33% drop in sphericity relative to the no field case at each temperature.

To determine the principal axis as a function of efield intensity, λ_x/λ_z, λ_y/λ_z, and λ_x/λ_y are reported for the 300 and 370 K simulations in Figure 8 and Figure 9 respectively. The ratio of λ_x/λ_z is well below unity for all nonzero efield intensities and temperatures simulated. However, λ_y/λ_z is only slightly below unity with $\lambda_y \approx \lambda_z$ for efield intensities less than 1.5 V/nm at 300 K, and less the 1 V/nm at 370 K. The ratio of λ_x/λ_y is a non-monotonic function of the efield intensity. For efield intensities below 1.5 V/nm, λ_x/λ_y is a decreasing function of the efield intensity. Here, $\lambda_x/\lambda_y < 1$, indicating that λ_x is the smallest eigenvalue, and that the x-axis is the principal axis of the nanoparticles grown under efield strengths 1 V/nm and below. At 1.5 V/nm, however, $\lambda_x/\lambda_y > 1$, indicating that the y-axis has become the principal axis during the 300 K simulations. This crossover appears to be thermally activated, as $\lambda_x/\lambda_y > 1$ for efield intensities 1 V/nm and 1.5 V/nm at 370 K.

The non-monotonic response of λ_x/λ_y is further captured in the w timeseries profiles for each efield intensity and temperature. Analysis of the w timeseries data in Figure 8d indicates that the crystal morphology adopted is dependent on the intensity of the applied electric field. In the case of the 300 K temperature simulations, w is an increasing function of the applied electric field intensity for electric field strengths below 1.5 V/nm and displays increasingly positive values indicative of increasingly cigar-like morphologies. However, w is observed to adopt negative values during the 1.5 V/nm intensity simulation, with an increasingly negative trend with increasing simulation length. Hence, the 1.5 V/nm intensity gives rise to increasingly plate-like crystal morphologies. At 370 K, w exhibits a large positive spike at short times under the 1.5 V/nm efield intensity, indicating that the morphology adopted by the nanocrystal prior to dissolution is strongly cigar-like.

Representative paracetamol nanocrystals grown in the 1 V/nm and 1.5 V/nm efield intensity efields at 300 K simulations are plotted in Figure 10. Visual inspection of the nanocrystal

DOI: 10.1021/acs.cgd.7b00356
Cryst. Growth Des. 2017, 17, 3751−3765

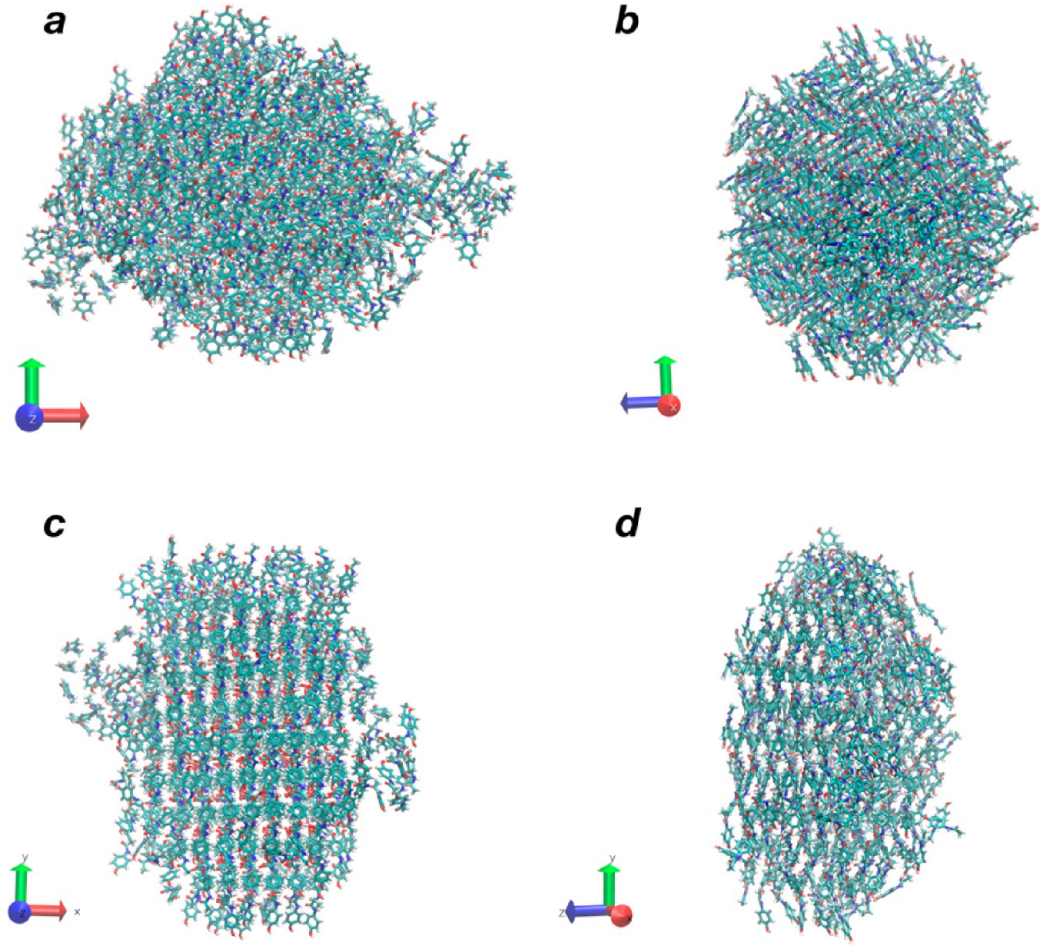

Figure 10. Representative nanocrystals grown in the presence of the 1 V/nm efield in (a) and (b), as well as the 1.5 V/nm efield in (c) and (d).

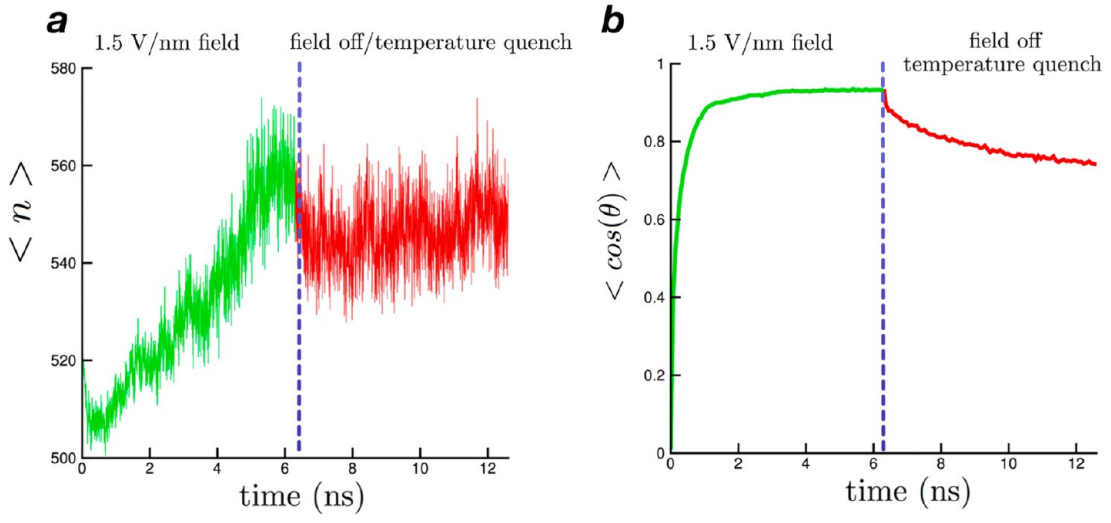

Figure 11. (a) Average number of solid molecules, $\langle n \rangle$, against time (ns), for 1.5 V/nm intensity efield until 6.3 ns at 300 K, followed by temperature quench to 245 K, the removal of the field, and an additional 6.3 ns of simulation. (b) $\langle \cos \theta \rangle$ of solid paracetamol molecules after the removal of the efield at 245 K.

reveals the different principal axis adopted under the two different field intensities. In the 1.5 V/nm efield intensity simulation, the nanocrystals compress along the x and z axis, giving rise to a more plate-like morphology in the presence of the efield vector. In the 1 V/nm efield intensity simulation, the nanocrystals elongate along the x-axis, with no distinction being given to the y or z axis. This shows that in addition to controlling the crystallization dynamics and polymorphic form that, the efield vector allows for manipulation of the crystal morphology.

3e. Temperature Quench Analysis. To investigate the stability of the newly produced polymorphic form, a temper-

DOI: 10.1021/acs.cgd.7b00356
Cryst. Growth Des. 2017, 17, 3751−3765

ature quench was performed in an attempt to prevent a solid state conversion when the efield in switched off. At 6.3 ns, the efield was turned off, and the temperature of the system was reinitialized to the new 245 K set point temperature as discussed in the computational details section. Higher temperatures than 245 K displayed dissolution and can be found in the Supporting Information Figure 3. The simulation was continued for an additional 6.3 ns in the absence of the field. In Figure 11a below, the average number of solid molecules vs time is plotted both with and without the presence of the efield. In Figure 11b, <cos θ> between solid paracetamol dipole vectors and the x-axis is plotted against time. Figure 11a demonstrates that over the additional 6.3 ns in the absence of the field, the system can be prevented from dissolving. However, Figure 11b demonstrates the newly produced polymorph nanocrystals exhibit a slow decay in alignment. In total, the system alignment decayed 17% over 6.3 ns of no field simulation. A similar slow transient recovery to the equilibrium condition in the absence of the field has also been observed in the response dynamics of SPC liquid water.[38] Even after 6.3 ns of no field, the nanocrystal still contains highly aligned paracetamol orientations, relative to the no field case that demonstrated zero average alignment in Figure 3. This demonstrates that reversion to the globally stable form I polymorph has not occurred completely. However, the transient decay in alignment in the absence of the electric field demonstrates that molecular dynamics predicts that pulsed electric fields during crystallization, or static fields applied over much longer time scales that those simulated herein, would be required to obtain micron sized crystals of the new polymorphic form.

The pharmaceutical industry is currently facing a bioavailability crisis, where 40−60% of all newly discovered drugs display poor aqueous solubility, and hence bioavailability, in vivo.[52,53] Even for a common drug such as paracetamol, both form I and form II are known to be sparingly soluble in aqueous solution.[7] As such, the target production of materials with improved aqueous solubility is readily sought in the industry. Methods to combat poor aqueous solubility include nanoparticle,[8,33,54,55] metastable,[7,56] and amorphous form production.[52,57,58] However, in this work, efield induced crystallization is predicted to allow for the formation of previously unobtainable, but metastable, polymorphic forms. Thus, we predict that efield crystallization presents a possible new method for the production of high bioavailability crystal lattices. The form discovered in this work is highly metastable, with a predicted melting temperature of approximately 245 K for the simulated nanocrystal size. This stands in contrast to the no-field simulation of form I, where the form I nanocrystal is shown to grow at 300 K. The melting temperature of a 2.9 nm form I nanocrystal in an equivalent concentration of dissolved paracetamol in water has recently been recently calculated to be 350 K in the absence of the efield.[59] In addition, the melting temperature of a 2.9 nm form II nanocrystal in an equivalent concentration of dissolved paracetamol in water was calculated to be 330 K.[59] This demonstrates that the newly produced polymorphic form is highly metastable relative to the two experimentally observed paracetamol low energy sturctures,[4] with a predicted melting temperature between 85 and 105 K lower than either form I or form II. The metastability of the newly produced polymorph corresponds to an increase in the solubility of the new form relative to form I and form II. As such, the new polymorph is predicted to be a promising candidate for increasing the bioavailability of paracetamol relative to form I and form II.

3f. Experimental Considerations. To date, the static efield strengths simulated herein remain 3−4 orders of magnitude larger than the static efield strengths previously applied to the crystallization of organic molecules in an experimental setting, where glycine crystallization from solution has been studied under a 0.0005 V/nm static efield intensity[60] and a 0.0006 V/nm static efield intensity.[61] To create the DC efield intensities simulated in this work, a 1000 times larger power source would be required to create the necessary ∼1 V/nm field intensity. Outside of DC efields, time dependent efield strengths are readily capable of reaching the intensity used in this work through the use of pico- to femtosecond lasers.[62] However, temporally varying fields give rise to increasingly relevant quantum mechanical effects, such as induced dipoles, which are not simulated in the force field used in this work. Alternatively, DC magnetic fields have recently demonstrated the ability to crystallize previously unknown polymorphic forms of coronene using 1 T magnetic field strengths.[51] This field strength is 20 times larger than previously applied magnetic field strengths of paracetamol,[24] leaving the possibility that larger, but ultimately currently accessible, DC magnetic field intensities may direct the crystallization of new polymorphs of paracetamol.

4. CONCLUSIONS

In this work, we study the ability of an externally applied efield vector to control not only the dynamics of a seeded crystallization process of paracetamol form I, but also the resulting polymorphic form and crystal morphology. A possible general phenomenon of MD predicting that crystalline structures produced from crystallization, in the presence of high intensity static efields, are materials that possess near perfect alignment with the applied efield vector is presented.

The crystallization growth dynamics at 300 K are impeded by the application of the efield, similar to results found in microwave paracetamol nucleation experiments.[24] Crystal growth rates show a roughly 40% depression relative to the no field case and show little to no variation with increasing efield intensity past 0.3 V/nm. The dissolution dynamics at 370 K are shown to be a strong, non-monotonic, function of the applied efield intensity. The fastest dissolution dynamics are observed with a 1 V/nm field intensity, resulting in a 200% increase in the dissolution rate relative to the no field dissolution rate. The dissolution dynamics then drop abruptly in the 1.5 V/nm intensity efield simulation, where the resulting dissolution rate at 1.5 V/nm intensity is 50% of the no field dissolution rate. As such, the efield vector is shown to be a strong external control variable for dissolution dynamics of paracetamol nanocrystals.

The calculated crystal growth and dissolution rates are subsequently justified through analysis of the $\langle\cos(\theta)\rangle$ dynamics for liquid and solid paracetamol molecules, where θ is the angle between the dipole moment of a paracetamol molecule and the applied efield vector. It is shown that liquid phase paracetamol molecules display rapid reorientation dynamics and achieve steady state alignment configurations within the first 25 ps. Solid state molecules however show sluggish response dynamics and frequently did not obtain steady state over the 6.3 ns simulation. This creates a kinetic competition between which phase can achieve spatial orientations with higher dipole alignment on the fastest time

DOI: 10.1021/acs.cgd.7b00356
Cryst. Growth Des. 2017, 17, 3751−3765

scale. In the case of crystal growth at 300 K, the solid paracetamol molecules only adopt orientations as favorable as the liquid in the 1.5 V/nm intensity simulation, rationalizing why the crystal growth rate is depressed for fields of lower intensity, as the liquid phase is preferentially stabilized due to higher alignment. In the case of dissolution, the solid paracetamol molecules again only adopt orientations as favorable in the liquid in the 1.5 V/nm intensity simulation. This rationalizes why the dissolution rate increases monotonically until 1.0 V/nm, as the liquid phase is stabilized preferentially to the solid, and then decreases at 1.5 V/nm, as the solid state is then preferentially stabilized relative to the liquid.

Analysis of the resulting nanocrystals grown from solution shows that the crystal retains the herringbone packing pattern characteristic of form I in both the efield and no field case. However, analysis of the probability distribution of $\langle \cos \theta \rangle$ between N−HN, O−C, and OH−HO bond vectors, and the efield vector, reveals that the paracetamol molecules adopt a new spatial orientation in the solid state, producing a new polymorph of paracetamol. In the new polymorphic form, paracetamol molecules are oriented such that the dipole moments of each paracetamol molecule in the solid state points directly down the efield vector. As key properties of a crystalline material are dictated by the final polymorph produced, we suspect the newly produced form will display markedly new properties in comparison to form I and form II.

The stability of the newly produced polymorph is studied through a temperature quench to 245 K. The solid state paracatamol molecules in the new polymorph show a slow exponential like decay in alignment, but remain significantly aligned over the short time scales simulated. The melting temperature of the new form is found to be approximately 245 K. As form I is shown to grow at 300 K in the absence of the efield, the 245 K melting temperature demonstrates the metastability of the newly produced polymorph. Given that paracetamol is sparingly soluble in aqueous solution, we have demonstrated that the newly produced form will exhibit increased aqueous solubility, and hence potentially increased bioavailability, relative to the currently manufactured form I of paracetamol.

■ ASSOCIATED CONTENT

Supporting Information

The Supporting Information is available free of charge on the ACS Publications website at DOI: 10.1021/acs.cgd.7b00356.

(1) AM1-BCC partial atomic charges used to simulate paracetamol molecules, (2) water RDFs at 300 K in the no field and 1.5 V/nm e-field intensity case, (3) order parameter validation, as well as (4) the temperature screening data used to estimate the melting temperature of the newly produced polymorph after the efield has been removed (PDF)

■ AUTHOR INFORMATION

Corresponding Author

*E-mail: ramkrish@ecn.purdue.edu.

ORCID

Zoltan K. Nagy: 0000-0003-4787-6678

Doraiswami Ramkrishna: 0000-0001-8158-5116

Notes

The authors declare no competing financial interest.

■ ACKNOWLEDGMENTS

This study was sponsored by AbbVie Inc. through Grant Number 8000053025 and 8000069224. H.-H.T. was an AbbVie employee at the time that he collaborated on this project. N.N. and S.B. are present employees of AbbVie Inc. This work used the Extreme Science and Engineering Discovery Environment (XSEDE), which is supported by National Science Foundation Grant Number ACI-1053575. This work used the XSEDE Extended Collaborative Support Service (ECSS) program. The authors would like to acknowledge XSEDE and Purdue RCAC, as all simulations were performed on Stampede supercomputer at TACC and Conte supercomputer at Purdue. The authors were given access to the Stampede supercomputer through XSEDE Grant CHE150072. The authors would like to acknowledge the tremendous help provided by Lei Huang and Yang Wang at TACC, and Xiao Zhu at Purdue, for their assistance in parallelizing the MD platform on Stampede and Conte.

■ REFERENCES

(1) Lee, A. Y.; Erdemir, D.; Myerson, A. S. *Annu. Rev. Chem. Biomol. Eng.* **2011**, *2*, 259−280.

(2) Nangia, A. *Acc. Chem. Res.* **2008**, *41*, 595−604.

(3) Bauer, J.; Spanton, S.; Henry, R.; Quick, J.; Dziki, W.; Porter, W.; Morris, J. *Pharm. Res.* **2001**, *18*, 859−866.

(4) Beyer, T.; Day, G. M.; Price, S. L. *J. Am. Chem. Soc.* **2001**, *123*, 5086−5094.

(5) Thomas, L. H.; Wales, C.; Zhao, L.; Wilson, C. C. *Cryst. Growth Des.* **2011**, *11*, 1450−1452.

(6) Gao, Y.; Olsen, K. W. *Mol. Pharmaceutics* **2014**, *11*, 3056−3067.

(7) Sudha, C.; Srinivasan, K. *CrystEngComm* **2013**, *15*, 1914.

(8) Jiang, Q.; Ward, M. D. *Chem. Soc. Rev.* **2014**, *43*, 2066−2079.

(9) Hamilton, B. D.; Hillmyer, M. A.; Ward, M. D. *Cryst. Growth Des.* **2008**, *8*, 3368−3375.

(10) Hamilton, B. D.; Ha, J.; Hillmyer, M. A.; Ward, M. D. *Acc. Chem. Res.* **2012**, *45*, 414−423.

(11) Rengarajan, G. T.; Enke, D.; Beiner, M. *Open Phys. Chem. J.* **2007**, *1*, 18−24.

(12) Garetz, B.; Aber, J.; Goddard, N.; Young, R.; Myerson, A. *Phys. Rev. Lett.* **1996**, *77*, 3475.

(13) Svishchev, I. M.; Kusalik, P. G. *Phys. Rev. Lett.* **1994**, *73*, 975−978.

(14) Svishchev, I. M.; Kusalik, P. G. *Phys. Rev. B: Condens. Matter Mater. Phys.* **1996**, *53*, R8815−R8817.

(15) Zaccaro, J.; Matic, J.; Myerson, A. S.; Garetz, B. A. *Cryst. Growth Des.* **2001**, *1*, 5−8.

(16) Sun, X.; Garetz, B. A.; Myerson, A. S. *Cryst. Growth Des.* **2008**, *8*, 1720−1722.

(17) Aber, J. E.; Arnold, S.; Garetz, B. A.; Myerson, A. S. *Phys. Rev. Lett.* **2005**, *94*, 145503.

(18) Towler, C. S.; Davey, R. J.; Lancaster, R. W.; Price, C. J. *J. Am. Chem. Soc.* **2004**, *126*, 13347−13353.

(19) Yan, J. Y.; Patey, G. N. *J. Phys. Chem. A* **2012**, *116*, 7057−7064.

(20) Yan, J. Y.; Overduin, S. D.; Patey, G. N. *J. Chem. Phys.* **2014**, *141*, 074501.

(21) Stan, C. A.; Tang, S. K. Y.; Bishop, K. J. M.; Whitesides, G. M. *J. Phys. Chem. B* **2011**, *115*, 1089−1097.

(22) Cheong, D. W.; Boon, Y. Di. *Cryst. Growth Des.* **2010**, *10*, 5146−5158.

(23) Wang, J.; Wolf, R. M.; Caldwell, J. W.; Kollman, P. A.; Case, D. A. *J. Comput. Chem.* **2004**, *25*, 1157−1174.

(24) Sudha, C.; Sivanarendiran, R.; Srinivasan, K. *Cryst. Res. Technol.* **2015**, *50*, 230−235.

(25) Parks, C.; Huang, L.; Wang, Y.; Ramkrishna, D. *Mol. Simul.* **2017**, *43*, 714−723.

(26) Parks, C.; Wang, Y.; Huang, L.; Ramkrishna, D. Github Repository; https://github.com/coparks2012/.

DOI: 10.1021/acs.cgd.7b00356
Cryst. Growth Des. 2017, 17, 3751−3765

(27) Greiner, M.; Elts, E.; Briesen, H. *Mol. Pharmaceutics* **2014**, *11*, 3009−3016.
(28) Berendsen, H. J. C.; van der Spoel, D.; van Drunen, R. *Comput. Phys. Commun.* **1995**, *91*, 43−56.
(29) Allen, F. H. *Acta Crystallogr., Sect. B: Struct. Sci.* **2002**, *58*, 380−388.
(30) Larsen, J. J.; Sakai, H.; Safvan, C. P.; Wendt-Larsen, I.; Stapelfeldt, H. *J. Chem. Phys.* **1999**, *111*, 7774−7781.
(31) English, N. J.; Waldron, C. J. *Phys. Chem. Chem. Phys.* **2015**, *17*, 12407−12440.
(32) Duff, N.; Peters, B. *J. Chem. Phys.* **2011**, *135*, 134101.
(33) Parks, C.; Koswara, A.; Tung, H.-H.; Nere, N. K.; Bordawekar, S.; Nagy, Z. K.; Ramkrishna, D. *Mol. Pharmaceutics* **2017**, *14*, 1023−1032.
(34) Parks, C.; Koswara, A.; DeVilbiss, F.; Tung, H.-H.; Nere, N. K.; Bordawekar, S.; Nagy, Z. K.; Ramkrishna, D. *Phys. Chem. Chem. Phys.* **2017**, *19*, 5285−5295.
(35) Lanaro, G.; Patey, G. N. *J. Phys. Chem. B* **2015**, *119*, 4275−4283.
(36) Blaak, R.; Auer, S.; Frenkel, D.; Löwen, H. *J. Phys.: Condens. Matter* **2004**, *16*, S3873−S3884.
(37) Sikora, M.; Szymczak, P.; Thompson, D.; Cieplak, M. *Nanotechnology* **2011**, *22*, 445601.
(38) Avena, M.; Marracino, P.; Liberti, M.; Apollonio, F.; English, N. J. *J. Chem. Phys.* **2015**, *142*, 141101.
(39) Zimmermann, N. E. R.; Vorselaars, B.; Quigley, D.; Peters, B. *J. Am. Chem. Soc.* **2015**, *137*, 13352−13361.
(40) Zaragoza, A.; Conde, M. M.; Espinosa, J. R.; Valeriani, C.; Vega, C.; Sanz, E. *J. Chem. Phys.* **2015**, *143*, 134504.
(41) Espinosa, J. R.; Sanz, E.; Valeriani, C.; Vega, C. *J. Chem. Phys.* **2014**, *141*, 18C529.
(42) Sanz, E.; Vega, C.; Espinosa, J. R.; Caballero-Bernal, R.; Abascal, J. L. F.; Valeriani, C. *J. Am. Chem. Soc.* **2013**, *135*, 15008−15017.
(43) Espinosa, J. R.; Vega, C.; Valeriani, C.; Sanz, E. *J. Chem. Phys.* **2016**, *144*, 034501.
(44) Bai, X.-M.; Li, M. *J. Chem. Phys.* **2006**, *124*, 124707.
(45) Abascal, J. L. F.; Fernández, R. G.; Vega, C.; Carignano, M. A. *J. Chem. Phys.* **2006**, *125*, 166101.
(46) Vega, C.; Sanz, E.; Abascal, J. L. F. *J. Chem. Phys.* **2005**, *122*, 114507.
(47) Geiger, P.; Dellago, C.; Macher, M.; Franchini, C.; Kresse, G.; Bernard, J.; Stern, J. N.; Loerting, T. *J. Phys. Chem. C* **2014**, *118*, 10989−10997.
(48) Sutmann, G. *J. Electroanal. Chem.* **1998**, *450*, 289−302.
(49) Knott, B. C.; Doherty, M. F.; Peters, B. *J. Chem. Phys.* **2011**, *134*, 154501.
(50) Yan, J. Y.; Patey, G. N. *J. Chem. Phys.* **2013**, *139*, 144501.
(51) Potticary, J.; Terry, L. R.; Bell, C.; Collins, A. M.; Fontanesi, C.; Kociok-Kohn, G.; Crampin, S.; Da Como, E.; Hall, S. R. *arXiv Prepr. Phys.*, 2015.
(52) Müller, R.; Junghanns. *Int. J. Nanomed.* **2008**, *3*, 295.
(53) Hasa, D. *Chem. Biochem. Eng. Q.* **2014**, *28*, 247−258.
(54) Keck, C.; Muller, R. *Eur. J. Pharm. Biopharm.* **2006**, *62*, 3−16.
(55) Beiner, M.; Rengarajan; Pankaj, S.; Enke, D.; Steinhart, M. *Nano Lett.* **2007**, *7*, 1381−1385.
(56) Di Profio, G.; Tucci, S.; Curcio, E.; Drioli, E. *Chem. Mater.* **2007**, *19*, 2386−2388.
(57) Hancock, B. C.; Parks, M. *Pharm. Res.* **2000**, *17*, 397−404.
(58) Williams, H. D.; Trevaskis, N. L.; Charman, S. A.; Shanker, R. M.; Charman, W. N.; Pouton, C. W.; Porter, C. J. H. *Pharmacol. Rev.* **2013**, *65*, 315−499.
(59) Parks, C.; Koswara, A.; Tung, H.-H.; Nere, N. K.; Shailendra, B.; Nagy, Z. K.; Ramkrishna, D. *Org. Process Res. Dev.*, submitted.
(60) Di Profio, G.; Reijonen, M. T.; Caliandro, R.; Guagliardi, A.; Curcio, E.; Drioli, E. *Phys. Chem. Chem. Phys.* **2013**, *15*, 9271−9280.
(61) Aber, J. E.; Arnold, S.; Garetz, B. A.; Myerson, A. S. *Phys. Rev. Lett.* **2005**, *94*, 1−4.
(62) Sommer, A.; Bothschafter, E. M.; Sato, S. A.; Jakubeit, C.; Latka, T.; Razskazovskaya, O.; Fattahi, H.; Jobst, M.; Schweinberger, W.; Shirvanyan, V.; Yakovlev, V. S.; Kienberger, R.; Yabana, K.; Karpowicz, N.; Schultze, M.; Krausz, F. *Nature* **2016**, *534*, 86−90.

DOI: 10.1021/acs.cgd.7b00356
Cryst. Growth Des. 2017, 17, 3751−3765